Coastal Engineering 69 (2012) 67–81

Contents lists available at SciVerse ScienceDirect

Coastal Engineering

journal homepage: www.elsevier.com/locate/coastaleng

Study of the turbulence in the air-side and water-side boundary layers in experimental laboratory wind induced surface waves

Sandro Longo [a,*,1], Luca Chiapponi [a], María Clavero [b], Tomi Mäkelä [b], Dongfang Liang [c]

[a] Department of Civil Engineering, University of Parma, Parco Area delle Scienze, 181/A, 43100 Parma, Italy
[b] Instituto Interuniversitario de Investigación del Sistema Tierra en Andalucía, Avda. del Mediterraneo s/n, 18006 Granada, Spain
[c] Engineering Department, University of Cambridge, Trumpington Street, Cambridge CB2 1PZ, UK

ARTICLE INFO

Article history:
Received 3 April 2012
Received in revised form 22 May 2012
Accepted 30 May 2012
Available online xxxx

Keywords:
Wind generated waves
Turbulence
Reynolds principal axes
Experiments

ABSTRACT

This study detailed the structure of turbulence in the air-side and water-side boundary layers in wind-induced surface waves. Inside the air boundary layer, the kurtosis is always greater than 3 (the value for normal distribution) for both horizontal and vertical velocity fluctuations. The skewness for the horizontal velocity is negative, but the skewness for the vertical velocity is always positive. On the water side, the kurtosis is always greater than 3, and the skewness is slightly negative for the horizontal velocity and slightly positive for the vertical velocity. The statistics of the angle between the instantaneous vertical fluctuation and the instantaneous horizontal velocity in the air is similar to those obtained over solid walls. Measurements in water show a large variance, and the peak is biased towards negative angles. In the quadrant analysis, the contribution of quadrants Q2 and Q4 is dominant on both the air side and the water side. The non-dimensional relative contributions and the concentration match fairly well near the interface. Sweeps in the air side (belonging to quadrant Q4) act directly on the interface and exert pressure fluctuations, which, in addition to the tangential stress and form drag, lead to the growth of the waves. The water drops detached from the crest and accelerated by the wind can play a major role in transferring momentum and in enhancing the turbulence level in the water side.

On the air side, the Reynolds stress tensor's principal axes are not collinear with the strain rate tensor, and show an angle $\alpha_\sigma \approx = -20^\circ$ to -25°. On the water side, the angle is $\alpha_\sigma \approx = -40^\circ$ to -45°. The ratio between the maximum and the minimum principal stresses is $\sigma_a/\sigma_b = 3$ to 4 on the air side, and $\sigma_a/\sigma_b = 1.5$ to 3 on the water side. In this respect, the air-side flow behaves like a classical boundary layer on a solid wall, while the water-side flow resembles a wake. The frequency of bursting on the water side increases significantly along the flow, which can be attributed to micro-breaking effects — expected to be more frequent at larger fetches.

© 2012 Elsevier B.V. All rights reserved.

1. Introduction

The theory of turbulent boundary layers assumes that the kinetic energy in the free stream is transferred to turbulent fluctuations and then dissipated into pure thermal energy by viscosity. The transfer process involves mean flow–turbulence interactions, turbulence–turbulence interactions and pressure–turbulence interaction. For wind turbulent boundary layer acting on water, as what happens in the ocean and lake, part of the wind stream energy is transferred into capillary and gravity waves and trigger water currents, vorticity and turbulence on the water side. The dominant role of wave breaking for current generation is confirmed by the evidence (Donelan, 1998) that over a broad wave-age range, $0.2 < c_p/U_a < 1.2$ (c_p is the phase celerity of the wave and U_a is a reference surface wind speed usually measured at the height $z = 10$ m above the interface), 95% of the wind momentum and energy flux is locally transferred to currents and only 5% propagates away in the form of waves. Hence a boundary layer beneath the interface is also generated on the water side, which exhibits some differences from the classical boundary layers.

Boundary layer flows are of importance to many engineering applications. In particular, wind-wave boundary layers are crucial in the transfer mechanisms for materials and energy at the ocean scale. Hence many efforts have been devoted to a better understanding of such a complex phenomenon. One aspect is the role played by coherent structures, even though most statistical descriptions and models of turbulence ignore their presence. The definition of coherent structure is itself a challenge. According to Robinson (1991), a coherent motion is defined as a three-dimensional region of the flow over which at least one fundamental flow variable (velocity component, density, temperature, etc.) exhibits significant correlation with itself or with another variable over a range of space and/or time that is significantly larger than the smallest local scales of the flow. Several other definitions are available in literature. Although not in an explicit way, many models do

* Corresponding author. Tel.: +39 0521 90 5157; fax: +39 0521 90 5924.
[1] Presently visitor at CUED, University of Cambridge, UK.

0378-3839/$ – see front matter © 2012 Elsevier B.V. All rights reserved.
doi:10.1016/j.coastaleng.2012.05.012

include the coherent structures in a hidden way. The simple non-diagonal components of the Reynolds stress tensor would be zero if a correlation between fluctuations were negligible. Hence even the most classical turbulence model admits some level of coherence amongst velocity fluctuations.

The major motivations for investigating coherent motions in turbulent boundary layers are to predict the gross statistics of turbulent flows, and to shed light on the dynamic phenomena responsible for the existence of statistical properties that we traditionally measure and predict through modelling.

There are also numerous other objectives, such as: (a) spatial and temporal characteristics and dynamic mechanisms related to the mixing between the two boundary layers; (b) spatial and temporal characteristics of large-scale outer-flow motions and their relation to entrainment; (c) causal direction and interactions between outer-flow motions and near-interface turbulence production, including the proper choice of scaling variables; and (d) relationship between fluctuating variables at the interface (pressure, wall shear, etc.) and the excitation of coherent motions through the frontier.

The correct identification of coherent structures would require instantaneous velocity measurements in several points at adequate data rate and spatial resolution. In most cases, all these requirements cannot be met simultaneously. Hence, the results are analysed to reveal the effects of coherent structures on the velocity statistics measured in a limited number of points, in most cases in 2D. Quadrant analysis is often used to quantify the mechanism of the exchange in the boundary layer. It is a conditional averaging method, in which the flow is classified according to the quadrant that the two velocity fluctuation components fall into (ejection, sweep, outward and inward interactions). It can be used to explore the Reynolds shear stresses' contribution to the momentum and energy balance. This analysis has been widely used in the wall boundary layer over a rigid wall (Alfredsson and Johansson, 1984), in the large-eddy simulation of the marine boundary layer (Foster et al., 2006) and in looking for the most significant form of disturbance (Nolan et al., 2010). It has already been used in the wind boundary layer experiments (Longo and Losada, 2012). Quadrant analysis and the boundary layer structure are inherently connected to intermittence. Intermittence is present at all length scales and describes the fluid velocity as a composition of a mean value – a time varying but almost deterministic component – and a purely random component. The second contribution is attributed to coherent structures. Coherent structures transport the purely random contribution by convection, which results in the flow field being partially or completely filled with turbulence. The consequence of the active presence of coherent structures and, hence, of intermittency is that the phenomenological turbulence model should not be based only on the characteristics of the mean flow, but should include the convective effects of the vortices at different length and time scales. It is true at both large scales and small scales, and has important implications on energy cascading in turbulence transfer mechanisms. Several researchers (e.g. Camussi and Gui, 1997) have demonstrated that, as a result of intermittency, the Kolgomorov scaling law is not completely correct, and that a signature of intermittency is the non-linear dependence of the exponent of the p-order velocity structure function on p.

The interest in turbulence analysis in the presence of waves is also due to the experimental evidence that a single parameter chosen to describe the interface geometry, e.g., the root mean square wave height, is inadequate in describing the characteristics of the wave boundary layer. Walls with identical roughness values can generate different turbulence, as reported for fixed walls (Krostad and Antonia, 1999) and also expected for mobile and interactive 'walls'. Hunt et al. (2011) analysed on the interaction of turbulence present on both sides of a gas–liquid interface. Brocchini and Peregrine (2001)describe the effects of turbulence scales on the liquid–gas interface geometry.

This paper complements a long-term activity on experimental analysis on laboratory wind-induced waves. In the previous papers (Longo, 2012; Longo and Losada, 2012; Longo et al., 2012) the mean water flow was analysed in detail, computing the friction velocity, the friction factor, the length scales in the water side, analysing the turbulence balance in the water side. The water wave characteristics were analysed, with details on their phase and group celerity, including the grouping analysis. Also the mean air flow and turbulence were analysed, with quadrant analysis and intermittence detection in the air side boundary layer. Herein the quadrant analysis in the water side boundary layer is performed and the statistics of the fluctuating velocities in the two facing boundary layers are compared, with the detection of the principal axes of the strain rate tensor and of the frequency of bursting.

The results of the past analyses shall be here briefly recalled in order to offer a complete self-contained overview of the experiments and of the main outcome. Also the results of measurements over a solid wall are recalled for comparison.

This paper is organised as follows: Section 2 shortly describes the experimental apparatus, the measurements and the main results. In Section 3, the measured statistics of turbulence is described, followed by the quadrant analysis in Section 4 and by the Reynolds stress tensor analysis in Section 5. In Section 6 the frequency of bursting is discussed.

The conclusions are presented in the last section.

2. Experimental apparatus and parameters

The experiments were conducted in a small non-closed low-speed wind tunnel in the Centro Andaluz de Medio Ambiente, CEAMA, University of Granada, Spain. The boundary layer wind tunnel is a poly(methyl methacrylate) (PMMA) structure with a test section that is 3.00 m in length with a 360 mm × 430 mm cross-section. The wind speed, up to 20 m/s, is controlled by a variable frequency converter controlling an electric fan at the downstream end with a maximum power of 2.2 kW. The air flow is straightened by a honeycomb section connected to the tunnel followed by a contraction. A water tank is installed to allow water wave generation. The water tank is constructed of PVC and is 970 mm in length and 395 mm high (internal size), while the still water depth is 105 mm. The overall layout is shown in Fig. 1. The air flow cross-section over the tank is 235 mm × 430 mm and is connected to the wind tunnel through an upstream ramp and a downstream ramp. One side of the tank is made of glass to allow optical access. The details of the layout of the wind tunnel and wave tank and definition of symbols are also shown in Fig. 1.

2.1. Velocity measurements and water level measurements

The wind speed in the tunnel and the water velocity in the water were measured with a TSI 2D Laser Doppler velocimetry (LDV) system in backward scatter mode. The laser source is an Innova 70 Series water-cooled Ar-Ion laser, which can reach a maximum power of 5 W. The measurement volume is defined by the intersection of the four laser beams, and has the shape of a prolate ellipsoid whose dimensions are ~0.08 mm × 0.08 mm × 1.25 mm.

The reference system for the transverse displacements and the velocity measurements has its horizontal origin ($x = 0$) at the upstream end of the water tank and its vertical origin ($z = 0$) at the still water level.

For measurements in the air, water droplets generated by a spray gun are used as seeding. The spray gun is outside of the wind tunnel, with the nozzle pointing towards the honeycomb section at the entrance of the wind tunnel. This setup ensures that the large water droplets are captured by the honeycomb section and that only the small drops reach the measurement section.

The water level has been measured using three different instruments: an ultrasound distance metre in the air, positioned on top of the wind tunnel, resistance probes in all the sections, and the echo output of the ultrasound Doppler velocity profiler.

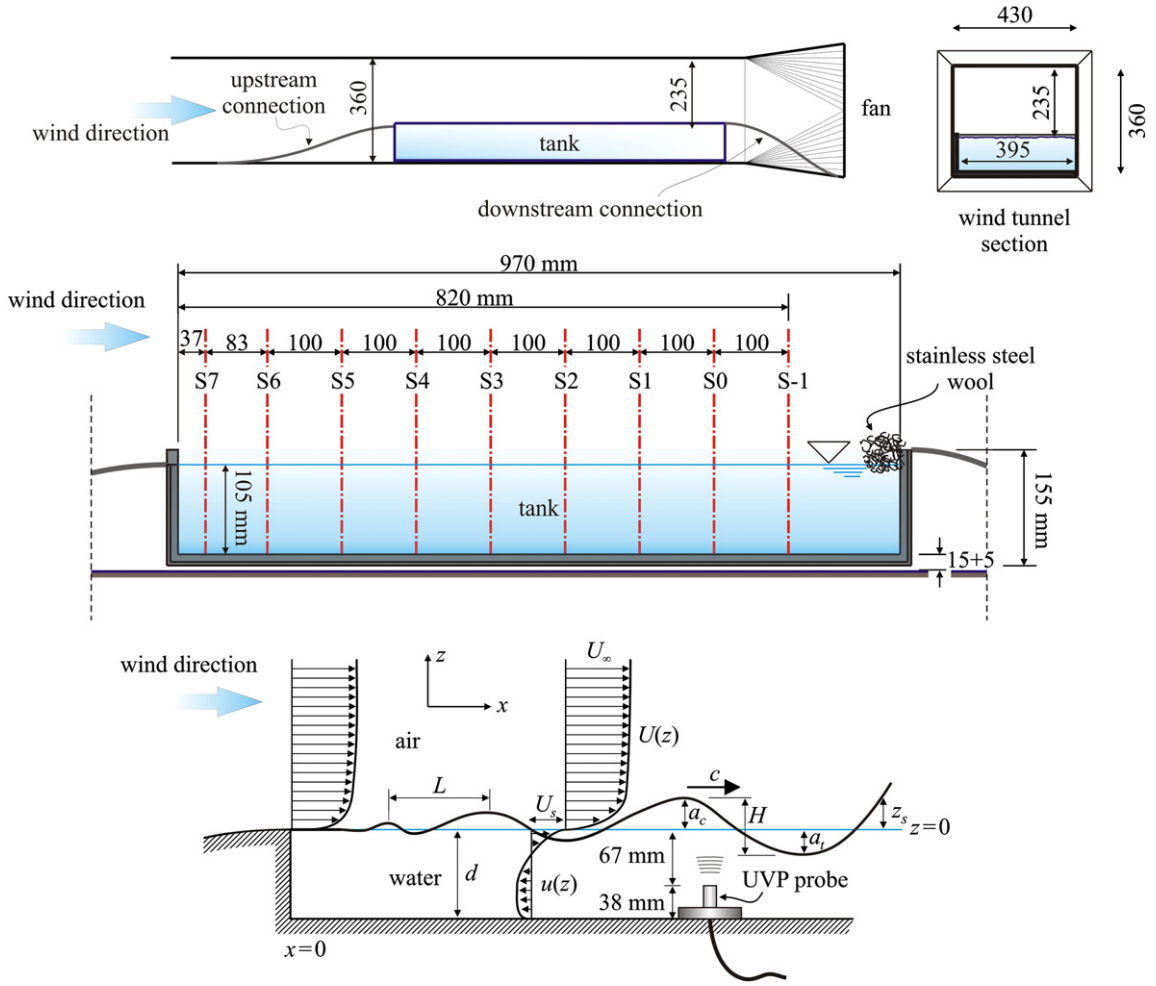

Fig. 1. Layout of the wind tunnel and of the wave tank.

For the free surface data analysis, the resistance probes are preferred, with data acquisition at a rate of 200 Hz through a DAQ board after filtering with a low-pass filter at 20 Hz. There are 8 resistance probes always connected and positioned in Sections from S7 to S0.

In addition also a set of measurements in air over a solid wall was carried out in Sections S0–S7 and used to check the overall performances of the wind tunnel after contraction. These measurements are frequently used in the present analysis for comparing the different behaviours of the wind stream in the presence of a flat surface and in the presence of a deformable surface.

All the details on these experiments can be found in Longo (2012), Longo et al. (2012), Longo and Losada (2012) and in Chiapponi et al. (2011).

The instantaneous velocity in air can be decomposed into a mean (time average) component $\overline{U}$and a fluctuating component U', which also includes the wave-induced contribution:

$$U(x,z,t) = \overline{U}(x,z) + U'(x,z,t). \tag{1}$$

The instantaneous velocity in water is decomposed into three components:

$$u(x,z,t) = \overline{u}(x,z) + \tilde{u}(x,z,t) + u'(x,z,t) \tag{2}$$

where $\overline{u}$ is the mean velocity, $\tilde{u}$ is the wave component and u' is the turbulent component. The mean velocity coincides with the ensemble velocity if the ergodic hypothesis holds. The separation of wave component is obtained by filtering the instantaneous velocity.

2.2. Results of the mean flows and surface waves

To analyse the air flow boundary layer, the fan speed was set at a specific value, resulting in a wind speed $U_\infty = 10.90$ m/s. The air velocity was measured at several points in Sections S0–S7, with a spacing of 1 mm near the interface and a larger spacing in the upper region. In a second series of tests, similar measurements were performed in water at four sections, S0–S3–S5–S6.

In both series the velocity exhibited a logarithmic profile. The adopted fitting curves on the air side are the law of wake:

$$(U_\infty + U_s - \overline{U})/u_{*a} = -1/k \ln(z/\delta) + (W_c/k)[2 - W(z/\delta)], \tag{3}$$

which can also be written as:

$$(\overline{U} - U_s)/u_{*a} = 1/k \ln(z u_{*a}/\nu_a) + C + (W_c/k)[1 - \cos(\pi z/\delta)] \tag{4}$$

where U_s is the surface drift approximated by $U_s = 0.55\ u_{*a}$, k is the von Karman constant, ν_a is the kinematic viscosity of air, U_∞ is the asymptotic velocity, u_{*a} is the friction velocity of the air stream, δ is the computed thickness of the boundary layer, W_c is the wake coefficient, $W(z/\delta) = 1 - \cos(\pi z/\delta)$ is the wake function.

The adopted fitting curves on the water side are:

$$(\overline{u} - U_s)/u_{*w} = 1/k \ln(z/k_s) + 8.5, \tag{5}$$

which can also be written as:

$$(\overline{u} - U_s)/u_{*w} = 1/k \ln(z u_{*w}/\nu_w) + C, \tag{6}$$

where u_{*w} is the friction velocity of the water stream, k_s is the roughness length, ν_w is the kinematic viscosity of water, and C is a parameter.

The main parameters were evaluated by a curve fitting procedure and are listed in Tables 1 and 2. Table 3 shows the main characteristics of the wind generated waves.

A synoptic description of the mean horizontal velocity profiles is illustrated in Fig. 2. For measurements on the air side, only those velocity profiles with their counterparts on the water side are shown.

3. The measured statistics of turbulence

Two important parameters about the variations of the fluctuating velocities are the kurtosis and the skewness, shown in Fig. 3 for the horizontal and vertical velocity components on the air side over a solid wall and over water.

For measurements over a solid wall, the kurtosis, a measure of the peakedness of the probability density function (p.d.f.), is in good agreement with the results in Kreplin and Eckelmann (1979) and Alfredsson and Johansson (1984), which are referred to KE and AJ data respectively. Measurements over water lie in a different range with respect to KE and AJ data, but are significantly different from the measurements over a solid wall. The value of the kurtosis is always greater than 3, which is the value for normal distribution.

The skewness is similar between tests over a solid wall and those over water, and follows the trend similar to that obtained by Kreplin and Eckelmann (1979) and Alfredsson and Johansson (1984). As a consequence of high speed fluid from the outer region, large positive events of U occur more frequently than the large negative events of U. The skewness for the horizontal velocity is negative over both solid wall and water, except in the outer region, where the Gaussian probability density distribution is reached. The skewness of the vertical velocity is always positive except for $z^+<50$, where it becomes negative over a solid wall. Large negative events of V are more frequent than large positive events of V. Similar results were also obtained by Nakagawa et al. (2003), who compared turbulent flows over a flat surface and over a surface with sinusoidal shapes of small wavelength.

The results with only the measurements on the water side are shown in Fig. 4. The kurtosis is always larger than 3, with higher values for the vertical velocity.

Skewness is slightly negative for the horizontal velocity and slightly positive for the vertical velocity except when $z^+<-300$. Beneath the interface, large positive values of u and large negative values of v are expected, which are also highly correlated as will be shown in the quadrant analysis in Section 4.

For shear flows over a boundary, the edge of the turbulent boundary layer is not sharp but constantly shifts in a region where turbulence becomes intermittent, as documented for the first time by Townsend (1948). We have verified using the present equipment that the distribution, $p(U')$, of the probability density of the velocity fluctuation in an isotropic turbulent flow is Gaussian. A higher kurtosis in the boundary layer will indicate that most of the variance is due to the infrequent extreme deviations hence kurtosis higher than 3 indicates fluctuating turbulence called intermittence.

Velocity measurements were also used to calculate the angle between the instantaneous vertical fluctuation and the instantaneous horizontal velocity. At any instant, the compound velocity vector is inclined at an angle $\beta_w = \tan^{-1}v'/(\overline{u}+u')$ in water and $\beta_a = \tan^{-1}V'/\left(\overline{U}+U'\right)$ in air. These values give indications on the direction of the momentum transfer. The normalized probability density distributions of these angles $p(\beta)$ are shown in Fig. 5 at different levels in the airside and waterside boundary layers. For comparison with data available in the literature, measurements over a solid wall are also shown. The present variations over a solid wall agree with the measurements given by other researchers (e.g. Kreplin and Eckelmann, 1979), with the maximum and minimum angles expected to be in the range $\beta_a = \pm 10°$. Similar results were also obtained by Antonia et al. (1990) in validating the X hot wire probe they used. They also found that the flow geometry was not affected by the Reynolds number Re_θ, at least in the range 1360–9630 in their tests.

The data in water show a larger variance of the distribution, and the peak is biased towards negative values. Considering that the horizontal velocity is mainly positive (except for $z>40$ mm due to the negative return current), the negative bias indicates that the turbulence dynamics in water mainly takes place in the fourth quadrant.

The change of angle of peak occurrence with the vertical position is shown in Fig. 6. The peak is slightly shifted to negative angles in the range 0° to −5° for airside measurements, but to much larger angles for the waterside measurements, where the peak reaches≈−30°

Table 2
The parameters for the mean water flow velocity profiles at different fetches. The measurements are in water. x is the fetch length, u_∞ is the asymptotic velocity in the water stream, u_{*w} is the friction velocity of the water stream, k_s is the roughness length, $Re_x = u_\infty x/\nu_w$ is the Reynolds number based on x and on u_∞, C is a parameter, δ_1 is the displacement thickness and θ is the momentum thickness, δ_1/θ is the shape factor of the boundary layer, $Re_\theta = u_\infty\theta/\nu_w$ is the Reynolds number based on momentum thickness, C_f is the friction coefficient.

Section #	S6	S5	S3	S0
x (mm)	120	220	420	720
u_∞ (m/s)	0.20	0.33	0.35	0.35
u_{*w} (m/s)	0.0095	0.0257	0.0318	0.0257
k_s (mm)	–	7.7	26.7	7.6
Re_x	24×10^3	77	147	252
C	5.5	−5.57	−8.34	−4.68
δ_1 (mm)	6.6	7.9	15.9	9.8
θ (mm)	3.4	4.5	9.3	4.6
δ_1/θ	1.94	1.75	1.71	2.13
Re_θ	1190	1575	3069	920
C_f	2.26×10^{-3}	5.39	8.26	5.39

Table 1
Parameters for mean air velocity profiles at different fetches. The measurements are in air over water. x is the fetch length, U_∞ is the asymptotic velocity, u_{*a} is the friction velocity, δ is the computed thickness of the boundary layer, W_c is the wake coefficient, $Re_x = U_\infty x/\nu_a$ is the Reynolds number based on x, C is a parameter, δ_1 is the displacement thickness and θ is the momentum thickness, δ_1/θ is the shape factor of the boundary layer, $Re_\theta = U_\infty\theta/\nu_a$ is the Reynolds number based on momentum thickness, C_f is the friction coefficient.

Section #	S7	S6	S5	S4	S3	S2	S1	S0
x (mm)	37	120	220	320	420	520	620	720
U_∞ (m/s)	10.30	10.50	10.93	10.72	10.74	10.72	10.94	10.92
u_{*a} (m/s)	0.39	0.40	0.74	0.71	0.68	0.72	0.63	0.63
δ (mm)	3.9	9.4	18.0	19.1	21.2	24.6	28.0	36.2
W_c	1.209	0.939	0.350	0.375	0.322	0.323	0.348	0.412
Re_x	0.252×10^5	0.834	1.59	2.27	2.99	3.69	4.49	5.21
C	8.84	7.76	−3.94	−3.78	−2.97	−4.39	−1.90	−2.95
δ_1 (mm)	0.8	2.4	4.1	4.6	4.3	5.6	6.3	7.7
θ (mm)	0.5	1.4	2.3	2.6	2.8	3.6	3.6	4.4
δ_1/θ	1.6	1.71	1.78	1.76	1.54	1.56	1.75	1.75
Re_θ	340	980	1675	1860	2005	2570	2630	3200
C_f	1.49×10^{-3}	1.51	4.95	4.72	4.30	4.86	3.54	3.55

Table 3
Statistics of waves generated in the wave tank. H_{rms} is the root mean square value of the wave height, L is the dominant wave length, f_p is the peak frequency, c_p is the phase celerity, c_g is the group celerity.

Section	S7	S6	S5	S4	S3	S2	S1	S0
x (mm)	37	120	220	320	420	520	620	720
H_{rms} (mm)	2.0	3.9	6.0	6.2	5.7	5.5	5.4	5.6
L (mm)	–	48 ± 4%	78	92	119	128	123	–
f_p (Hz)	–	6.20 ± 0.025	5.18	5.27	4.25	3.91	4.25	3.61
c_p (m/s)	–	0.30 ± 3.5%	0.40	0.48	0.51	0.50	0.52	3.61
c_g (m/s)	–	–	0.31 ± 3.5%	0.36	0.41	0.41	0.39	–

and≈−40° at Sections S3 and S0, respectively. Different behaviours of the boundary layers are observed: in air (over either a solid wall or over water), the p.d.f. near the interface is broadened, whereas, in water, the broadening occurs far from the interface. Indeed, the flow stream on the water side does not experience a laminar outer region. The region where water or air is present only for a fraction of the time is indicated by the dashed area, with $a_{c\text{-}rms}$ and $a_{t\text{-}rms}$ representing the root mean square values of the crests and the troughs respectively (see Table 1 in Longo, 2012). In this region the symbols report the time averaged values.

4. Quadrant analysis

Insight on the structure of momentum exchange due to turbulence can be gained by the quadrant analysis. To reveal the structure of turbulence, Reynolds shear stress contributions are categorised according to their origin, and are divided into four quadrants. Then, conditionally sampling according to the quadrant categorisation gives the statistics of the classified events, as shown in Fig. 7. Due to the reference system adopted, we keep the number for the quadrants based on the sign of the fluctuating components as usually adopted,

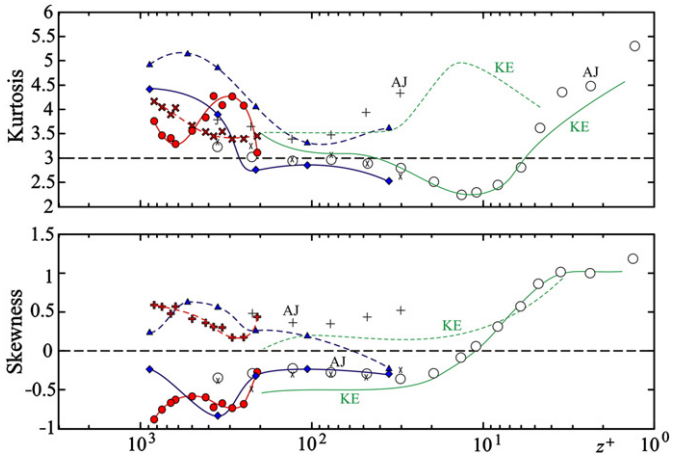

Fig. 3. Distribution of the statistical moments. Present tests, Section S0: measurements in air over a solid wall, ◆U; ▲V; measurements in air over water: ●U; ✚V. Data from Alfredsson and Johansson (1984): X and ○ (single probe) for U, + for V. Data from Kreplin and Eckelmann (1979): –, U; ---,V.

but rename the coherent structures in different quadrants in order to be consistent with the denomination adopted in a standard boundary layer. For example, an ejection is defined as outward movement of low-speed fluid, which belongs to quadrant Q2 for the standard case, but, in the present boundary layer in the waterside, it belongs to quadrant Q3; sweep is high-speed fluid moving towards the wall, including inrushes from the outer region which belongs to quadrant Q3 for the standard case, but, in the present context for the waterside, it belongs to quadrant Q1.

Ejections and sweeps are generally the main contributors to the transfer of momentum in a turbulent boundary layer. The event-averaged shear stress for the ith quadrant is computed as:

$$\langle \overline{u'v'} \rangle_i = \frac{1}{N_i} \sum_{j=1}^{N_i} \left[u'v' \right]_{j,i} \text{ for } i = 1, \ldots, 4, \tag{7}$$

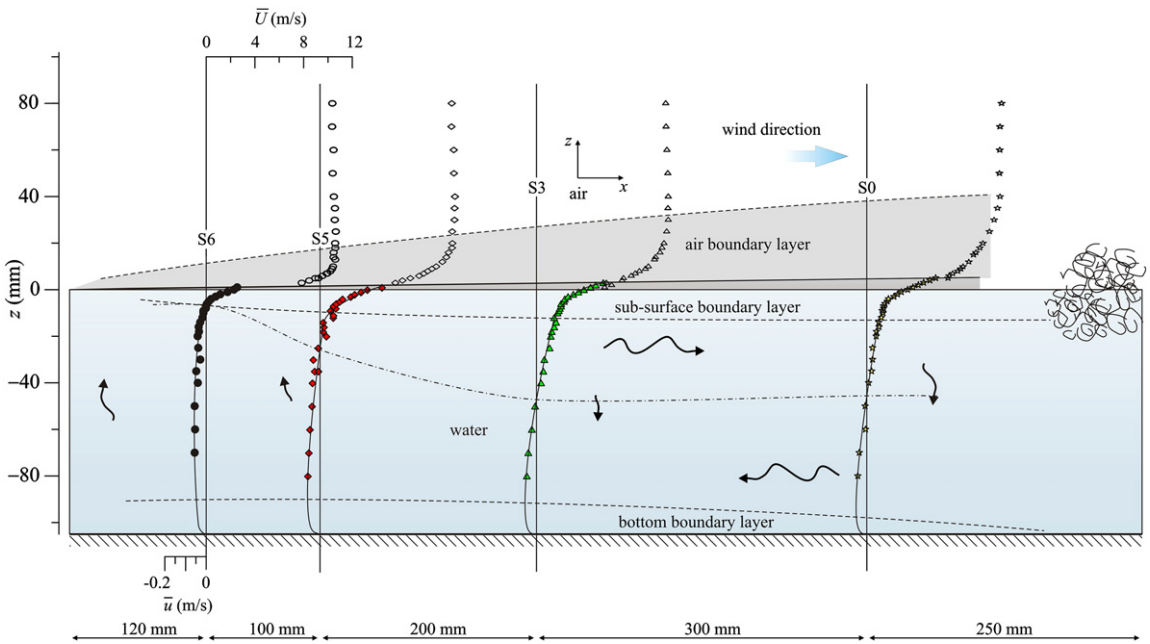

Fig. 2. Synoptic view of the horizontal velocity profiles in water (filled symbols) and in air (empty symbols). The dark grey area marks the domain where water waves are present allowing velocity measurements in water. The dashdot curve is the trace of the surface of zero horizontal velocity defining the limit between the drift positive current and the undertow current. The velocity scales are different for waterside and airside velocity.

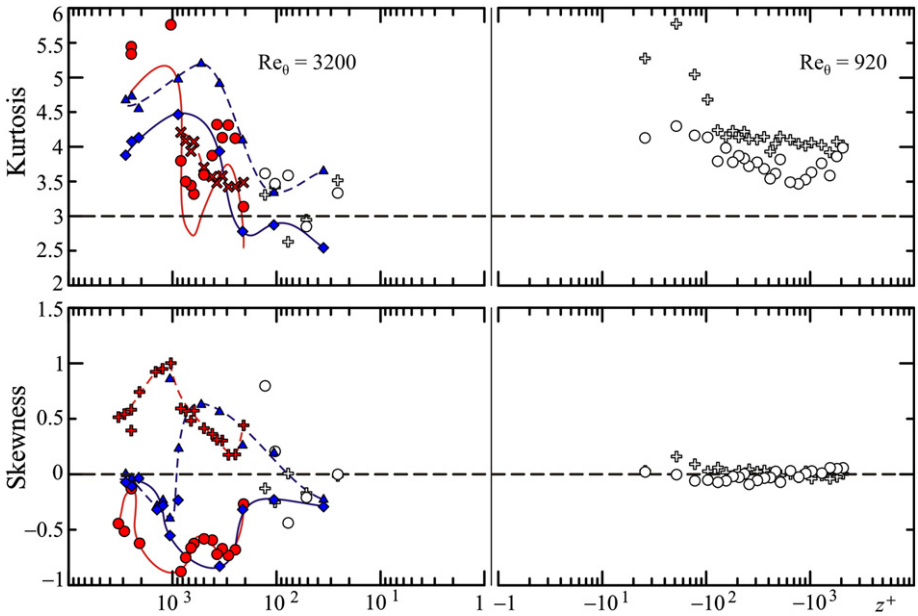

Fig. 4. Distribution of the statistical moments, Section S0: measurements in air over a solid wall, ◆ U; ▲ V; measurements in air over water: ● U; ✚ V; measurements in water, ○ u; ✣ v.

where N_i is the number of events in the ith quadrant and j is the current sample number. The average shear stress for the ith quadrant is

$$\overline{u'v'}_i = \frac{1}{N}\sum_{j=1}^{N_i}\left[u'v'_j\right]_i \text{ for } i = 1,\ldots,4. \tag{8}$$

The ratio, N_i/N, is the relative permanence of the events in the i-quadrant, hence

$$\overline{u'v'}_i = \frac{N_i}{N}<\overline{u'v'}>_i \tag{9}$$

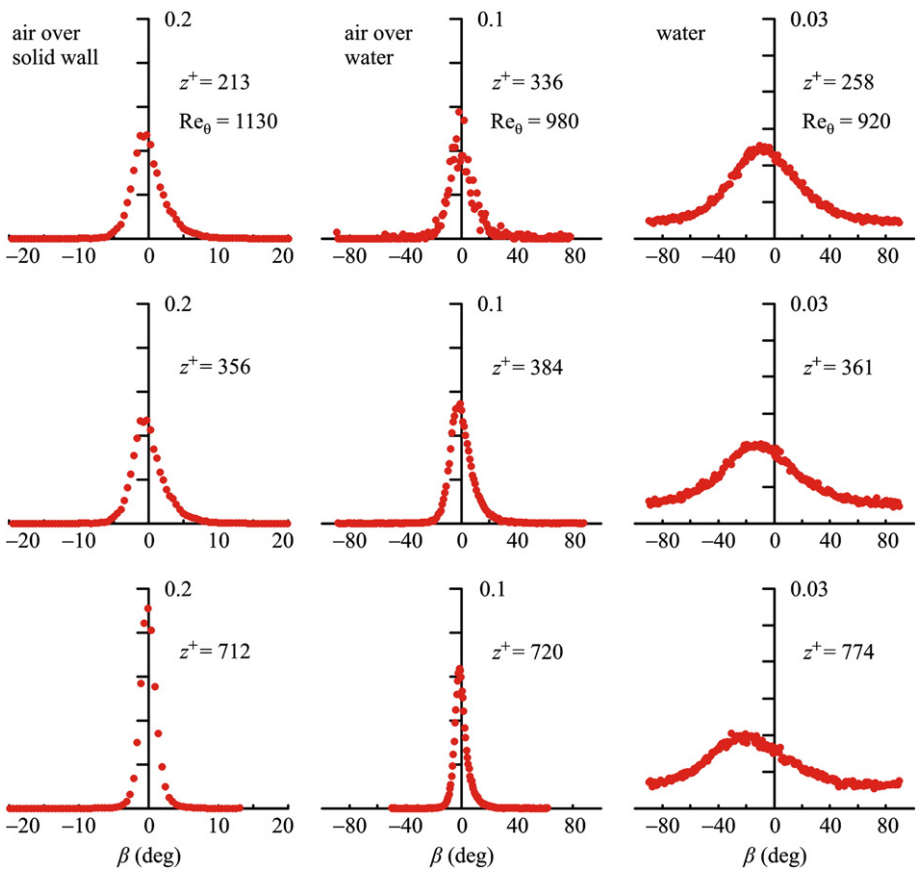

Fig. 5. Probability density distribution of the angle between the instantaneous values of the vertical velocity fluctuation and the horizontal velocity at different distances from the interfaces, in the airside over a solid wall (left panels), in the airside over water (central panels) and in the waterside (right panels). Measurements in Section S0 in water and in air over a solid wall, in Section S2 in air over water. The vertical scale is different for the three series, the horizontal scale is different for measurements in air over a solid wall.

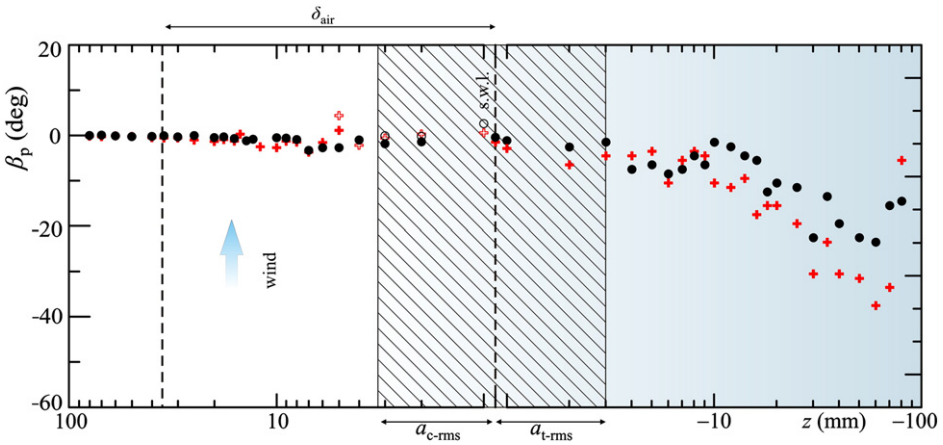

Fig. 6. Measurements in air over water and in water. Angle of peak occurrence of probability density distribution of the angle between the instantaneous values of vertical velocity fluctuations and horizontal velocity. ✚: Section S0, ●: Section S3. The empty symbols refer to measurements in water above the still water level. $a_{c\text{-rms}}$, $a_{t\text{-rms}}$ is the root mean square value of the crests, of the troughs.

and the total shear stress is

$$\overline{u'v'} = \sum_{i=1}^{4} \overline{u'v'}_i. \tag{10}$$

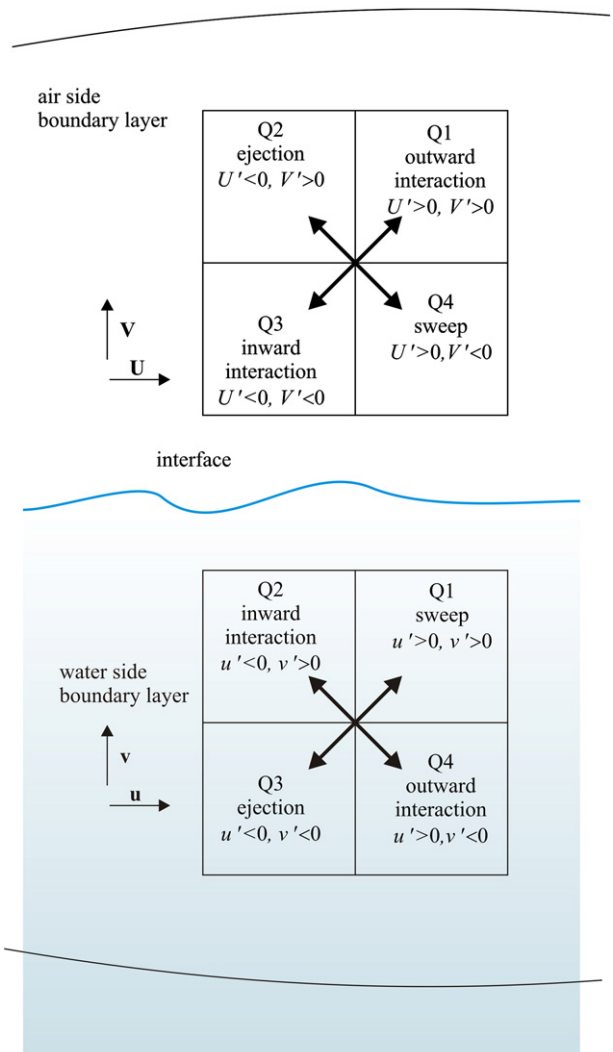

Fig. 7. Quadrant decomposition of the fluctuating components of velocity.

It is of interest to restrict the analysis to values above a fixed threshold. These values indicate the presence of coherent structures carrying a significant momentum in the boundary layer. The threshold is usually defined as:

$$\left|u'v'\right| > Hu'_{rms}v'_{rms} \tag{11}$$

where H is a threshold. The concentration of the ith quadrant for a fixed threshold level is

$$C_H^i = \frac{1}{N}\sum_{j=1}^{N} \phi_{Hj}^i, \tag{12}$$

where

$$\phi_{H,j}^i = \begin{cases} 1 \text{if} \left|u'v'\right|_j > Hu'_{rms}v'_{rms} \text{ and belongs to the } i-\text{quadrant} \\ 0 \text{ otherwise} \end{cases} \tag{13}$$

We can also consider the phasic-averaged Reynolds stress for the ith quadrant:

$$\left(\widehat{u'v'}\right)_H^i = \frac{\sum_{j=1}^{N}\left(u'v'\right)_j \phi_{H,j}^i}{\sum_{j=1}^{N}\phi_{H,j}^i}, \tag{14}$$

and the time-averaged Reynolds stress for the ith quadrant:

$$\left(\overline{u'v'}\right)_H^i = \frac{1}{N}\sum_{j=1}^{N}\left(u'v'\right)_j \phi_{H,j}^i = C_H^i\left(\widehat{u'v'}\right)_H^i \tag{15}$$

also expressed in the non-dimensional form as stress fraction:

$$S_H^i = \left(\overline{u'v'}\right)_H^i \overline{u'v'}. \tag{16}$$

Furthermore,

$$S_0^1 + S_0^2 + S_0^3 + S_0^4 = 1. \tag{17}$$

The conditional averages are strictly related to the joint probability density function of the fluctuating velocities. In Fig. 8, the fluctuating velocities' p.d.f. for measurements in water is shown at three levels. The contours, with a constant interval of each 10%, are elliptic with the major axis along the bisector of quadrants Q2 and Q4 at the interface

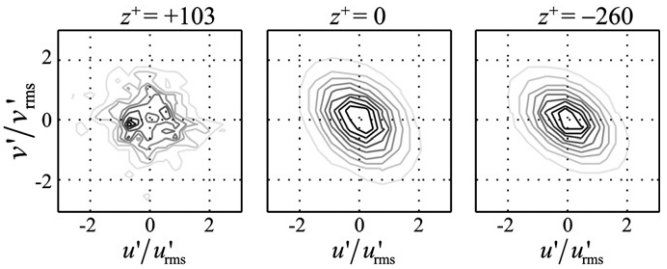

Fig. 8. Joint probability density function of the fluctuating velocities at three different heights above the still water level. Contours denote probabilities variation of 10%, the most internal curve is equal to 90%. Data refer to measurements in water, Section S0.

and at levels beneath the interface, indicating that the fluctuations tend to inhibit each other in the first and the third quadrants. For measurements above the still water level, the correlation is weaker, and contours seem to be uniformly distributed.

Similar p.d.f. on the air side has been observed, as reported in Fig. 15 of Longo and Losada (2012). This shows that, near the edge of the airside boundary layer, turbulence appears to be isotropic, whereas, near the interface, it becomes elliptic with sweeps dominant.

The Reynolds shear stress measurements are shown in Fig. 9a for Section S0, with a threshold $H=1$. The data show the extent to which each quadrant contributes to the overall stress in a time-averaged sense. The two major contributors are quadrants Q2 and Q4, which are associated with the events called inward and outward interactions in the waterside boundary layer. They both peak at the boundary layer limit with $z/\delta \approx -1$, whereas the contributions from the first and the third quadrants, associated with sweep and ejection, peak at $z/\delta \approx -0.30$. The peaks in Q2 and Q4 are more than 3 times greater than those in Q1 and Q3.

Fig. 9b shows the concentration of the Reynolds stress and the contribution from each quadrant, where they all peak at $z/\delta < -1$. Some measurements are above the still water level, and they show a progressive reduction of intensity with a spike near the last measurement points. At $z/\delta \approx +0.30$, the four quadrants give almost the same contribution.

Figs. 10 and 11 show the conditional distributions of the Reynolds stresses in both air and water. The data on the air side have been partially analysed in Longo and Losada (2012), and are herein more extensively presented together with that data on the water side.

Quadrants Q2 and Q4 are dominant contributors to the net turbulence stress. A threshold of $H=1$ was selected in the calculations. Across the interface, the non-dimensional quadrant contribution does not experience any significant discontinuity of the relative intensity, at least for the quadrants with most contributions. Sweeps and ejections in the wind boundary layer progress as inward and outward interactions in the water-side boundary layer, and both concentration and time-averaged non-dimensional values match together. With increasing fetch, moving from Section S3 to Section S0, the contribution from Q2 and Q4 on the water side becomes larger, but the vertical distribution remains similar and the concentration is nearly equal to 10%. Q1 and Q3 account for less than 3% each. Close to the interface where crests and troughs of the gravity waves alternate, all the variables are smoothed as a consequence of the average performed: the time-average also takes into account the interval with the absence of the relevant phase (due to the presence of wave crests for measurements in air, and the presence of troughs for measurements in water). The results are found to be only slightly sensitive to the threshold value H.

An important parameter to describe the joint probability density function is the value $\Delta S_0 = S_0^4 - S_0^2$, which is the difference between the non-dimensional conditional stresses in quadrants Q4 and Q2 without threshold. Raupach (1981) has demonstrated that, for turbulent boundary layers outside the roughness sub-layer, the statistics of the velocity fluctuations can be succinctly described by this parameter alone, which can be completely evaluated in terms of the third order moments of u' and v'. ΔS_0 is shown in Fig. 12 at the two Sections S3 and S0. On the air side, present measurements give results similar to Raupach's results above a solid wall. On the water side, however, there are several differences from Raupach's analysis. The contribution of the second quadrant (sweep) is generally dominant on the air side. This is also true immediately beneath the interface (inward interaction), but, far from the interface, the main contribution is due to quadrant Q4 (outward interaction). The unbalance in water is much smaller than that on the air side.

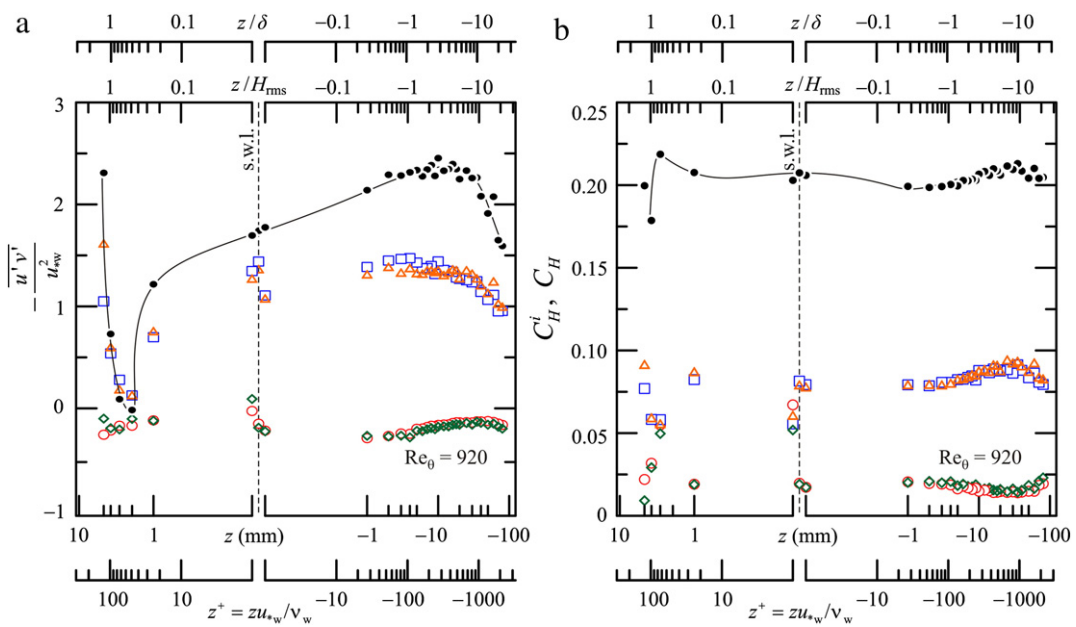

Fig. 9. Measurements in water, Section S0. a) Time-averaged Reynolds shear stress with threshold $H=1$ (symbol ●) and quadrant decomposed; b) concentration. ○ Q1 (sweep), □ Q2 (inward interaction), ◇ Q3 (ejection), △ Q4 (outward interaction). The description of the contribution for the four quadrants is different from the classical due to the inverted vertical axis in the water side boundary layer.

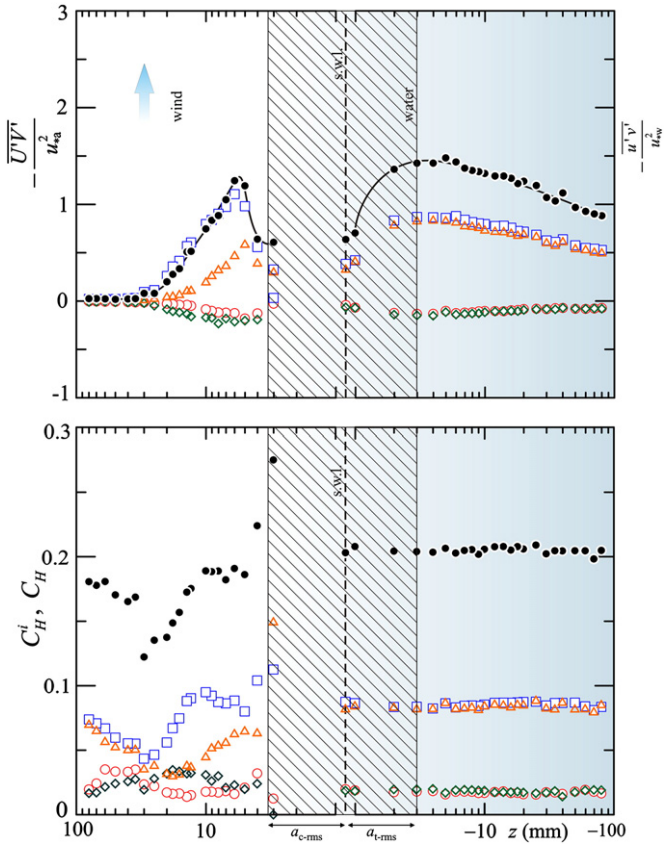

Fig. 10. Measurements in air over water and in water, Section S3. Upper panel: time-averaged Reynolds shear stress with threshold $H=1$ (symbol ●) and quadrant decomposed; lower panel: concentration. ○ Q1, □ Q2 , ◇ Q3, △ Q4. $a_{c\text{-}rms}$, $a_{t\text{-}rms}$ is the root mean square value of the crests, of the troughs.

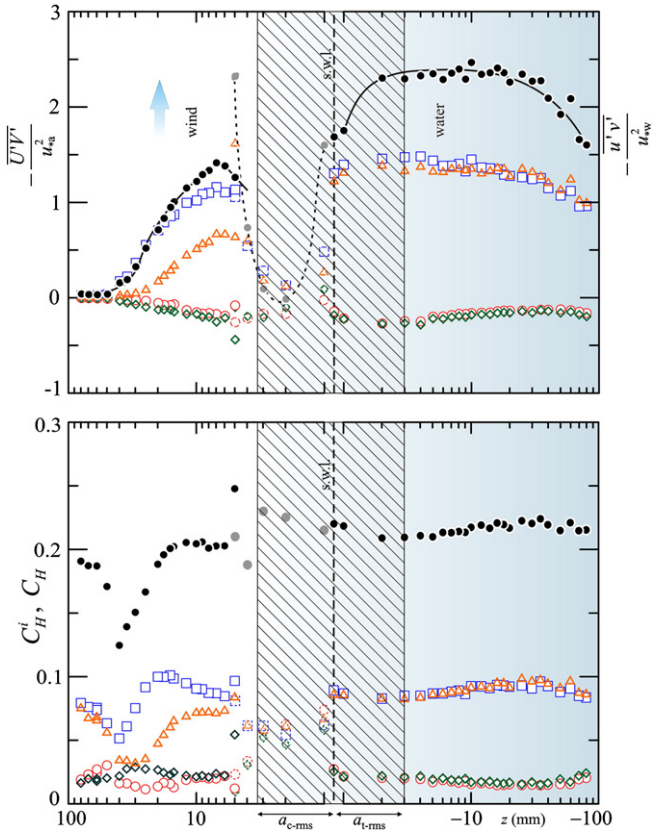

Fig. 11. Measurements in air over water and in water, Section S0. Upper panel: time-averaged Reynolds shear stress with threshold $H=1$ (symbol ●) and quadrant decomposed; lower panel: concentration. ○ Q1, □ Q2 , ◇ Q3, △ Q4 . Dashed and grey symbols refer to measurements in water above the still water level. $a_{c\text{-}rms}$, $a_{t\text{-}rms}$ is the root mean square value of the crests, of the troughs.

The relative time averaged intensity of the Reynolds shear stress on the water side for different threshold H is shown in Figs. 13 and 14 for Sections S3 and S0. Quadrants Q2 and Q4 are always dominant, like that on the air side (Longo and Losada, 2012). The inward interaction coherent structures, in the form of retarded streaks moving upward towards the interface, gain momentum and transfer it to the liquid with a concentration greater than 5% for $H=1$. The contribution of the outward interaction is of almost the same magnitude, whereas the other two quadrants give negligible contribution. The duration of inward and outward interaction at $z/\delta\approx -0.1$ (or $z/H_{rms}\approx -1$) is slightly less than 1% with a threshold $H=5$, but the contribution is still ≈30% of the total stress. Therefore, the process is significantly intermittent. In the wave crest, the duration of the events is larger than at the still water level, but their intensity (time average) is limited. The phasic-average, computed only when water is present, should give much larger values.

The dominant coherent structures are continuous through the interface, and they shed light on the mechanism of transmission of energy and momentum from the wind to the water. The impulsive action of ejections in the airside boundary layer (belonging to quadrant Q2) tends to generate the defect momentum in the near interface region and gain energy from the macrovortices. Sweeps (belonging to quadrant Q4) act directly on the interface and exert pressure fluctuations, which, in addition to the tangential stress and form drag, lead to the growth of the waves. In the boundary layer beneath the interface, the outward interactions (still belonging to quadrant Q2) bring the momentum defect in regions where the turbulent waves and the currents are active. Outward interactions (quadrant Q4) transfer the excess of momentum to water current. The level of correlation between Q2–Q4 coherent structures cannot be verified in the present study, since measurements are not concurrent, but it is expected to be quite high and dependent on the age of the wave. We also expect a significant influence of the micro-breaking, defined as breaking of relatively short waves without air entertainment, since it is responsible for the transfer of a large proportion of energy. Micro-breaking should be equivalent to sweeps (quadrant Q4) in the airside boundary layer.

A second source of momentum is the spray and the cloud of drops detached from the wave crest if strong wind blows. According to Kudryavtsev (2006), a realistic picture presumes that, as a result from mechanical tearing of wave crests, spume drops are ejected horizontally at altitudes of breaking crests. These have the effect to significantly reduce the surface drag, but effectively transfer momentum in the water layer by impact. This effect was analysed by Andreas (2004) who evaluated the flux of momentum associated with spray. In the present experiments spray action should not be important, since the wind speed is not very high, and we expect that drop detachment from the crest should play a major role.

If we assume that, due to the wind action, the fraction of crest detached is equal to $(1-\chi)$, the mass discharge of water per unit wavelength and unit width of the wave front is equal to

$$\rho H \frac{\sqrt{1-\chi^2}-\chi\cos^{-1}\chi}{2\pi}. \tag{18}$$

Choosing a control volume moving with the surface drift, the momentum flux per unit surface towards the liquid phase is equal to

$$\rho \frac{H}{L} \frac{\sqrt{1-\chi^2}-\chi\cos^{-1}\chi}{2\pi} (U_d-U_s)^2 \tag{19}$$

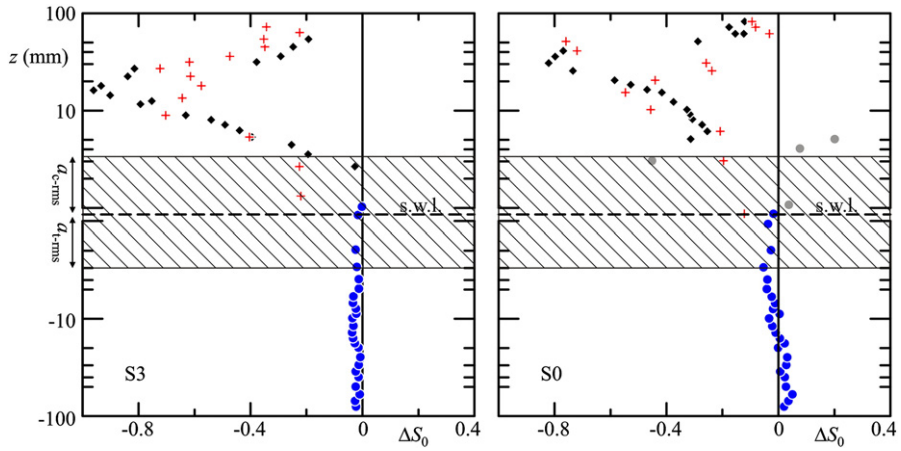

Fig. 12. The difference ΔS_0 between Q4 and Q2 stress contributions for the two Sections S3 and S0: + measurements over a solid wall; ♦ measurements in air over water; ● measurements in water. Grey symbols refer to measurements in water above the still water level. $a_{c\text{-rms}}$, $a_{t\text{-rms}}$ is the root mean square value of the crests, of the troughs.

where U_d is the velocity of the detached drops when impinging on the liquid surface. The non-dimensional form results:

$$\frac{\tau_{mb}}{\rho u_{*w}^2} = \frac{H}{L}\frac{\sqrt{1-\chi^2}-\chi\cos^{-1}\chi}{2\pi}\left(\frac{U_d - U_s}{u_{*w}}\right)^2. \tag{20}$$

Considering the data in Section S0 and assuming that the velocity of the detached drops is equal to the phase celerity and that the reduction of the wave crest due to spray and droplet generation is equal to 10%, substituting in Eq. (20) results in the following stress per unit mass density

$$\tau_{mb} = \frac{5.4\times10^{-3}}{0.123}\frac{\sqrt{1-0.9^2}-0.9\cos^{-1}0.9}{2\pi}\left(\frac{0.52-0.55\times0.63}{0.0257}\right)^2 \approx 0.01\,u_{*w}^2 \tag{21}$$

It is a small value, similar to that obtained by the Andreas (2004) model for spray. A strong increment is obtained by assuming that the droplets, once detached, are accelerated by the fast wind stream. Indeed they can easily reach the wind speed before falling if their radius is sufficiently small. If their velocity at impact is equal to 1 m/s, the contribution becomes $\tau_{mb}\approx 0.14\,u_{*w}^2$, which starts to be significant. If $U_d = 2$ m/s, then $\tau_{mb}\approx 0.86\,u_{*w}^2$, which is definitely significant. The force necessary to accelerate the droplets is already included in the friction of the wind, and does not change the drag. For small droplets, the acceleration due to the wind can be much stronger, so the fast droplets can transfer a larger amount of momentum, even though the violent aeration vaporizes part of the detached mass.

5. Reynolds stress tensor's principal axes

The interaction between the mean motion and the fluctuating velocity can be analysed observing the Reynolds stress tensor. The simplest experiment concerning the response of the principal axes of the Reynolds stress tensor to the external flow field is the action of a constant pure plane strain on an initially isotropic turbulence (Townsend, 1954; Tucker and Reynolds, 1968). In that case, the principal axes of the Reynolds stress tensor are those of the mean rate of strain, and the turbulent motion appears as 'oriented' by the strain field. If the strain field changes, the axes of the Reynolds stress tensor have a tendency to be reoriented along the axes of the new strain, with a delay related to a relaxation time of the order of the time scale of the imposed strain. If the strain tensor reduces to a pure shear stress, several experiments (e.g. Harris et al., 1977) show that, for isotropic turbulence, the principal axes of the Reynolds stress tensor are not aligned with those of the strain, which is a consequence of the mean rotation. In Harris et al. (1977) experiments, a sudden variation of a pure strain is applied to grid-generated turbulence. These results should be midway between those with constant uniform strains and those with pure uniform shears. In fact, a constant shear situation can be composed by superposing a pure plane strain on a mean rotation. Hence, the action of the constant shear is equivalent to one of a pure plane strain, the principal axes of which instantaneously rotate around an axis perpendicular to the plane of the strain. The characteristic time of the mean rotation and the associated strain is twice the characteristic time of the shearing, i.e. the relaxation time of re-orientation of the Reynolds stress tensor. Hence, in shearing, the principal axes of the Reynolds stress tensor cannot be aligned with those of the associated strain, which make a 45° angle with the direction of the flow, even though the tendency is towards a complete re-alignment. The general picture shows that the principal axes of the two tensors are not collinear. The co-linearity is closely related to a common model of turbulence, which relates the Reynolds stress tensor to the strain rate tensor in a linear Newtonian fashion:

$$-\overline{u'_i u'_j} + \frac{2}{3}\kappa\delta_{ij} = \nu_t\, S_{ij} \tag{22}$$

where κ is the turbulent kinetic energy, ν_t is the eddy viscosity and S_{ij} is the strain rate tensor. The over bar indicates the correlation. This is an isotropic algebraic constitutive relation that works fairly well for wakes but less well for many other flows. The orientation found in the boundary layer and channel flow is (see Champagne et al., 1970) $\alpha_\sigma \approx -20°$ to $-25°$ and 70° to 65°, while that in the wake is $\alpha_\sigma \approx 40°$ to 50° and $-50°$ to $-40°$. In both cases, the principal axes of the strain rate tensor are $\alpha_D = \pm 45°$. Also, the ratio of the maximum–minimum stresses is the characteristic of specific flows. The two principal stresses in the x–z plane are

$$\sigma_{a,b} = \frac{\overline{u'u'} + \overline{v'v'}}{2} \pm \sqrt{\left(\frac{\overline{u'u'} - \overline{v'v'}}{2}\right)^2 + \left(\overline{u'v'}\right)^2} \tag{23}$$

and their ratio is (see Champagne et al., 1970):

$$\left.\begin{array}{rll} \text{boundary layer}: & \sigma_a/\sigma_b = & 3 \text{ to } 4 \\ \text{channel}: & \sigma_a/\sigma_b = & 3 \text{ to } 5 \\ \text{plane wake}: & \sigma_a/\sigma_b = & 2 \text{ to } 6 \end{array}\right\} \tag{24}$$

The present experiments results in $\sigma_a/\sigma_b = 1.5$ to 3 on the water side and $\sigma_a/\sigma_b = 3$ to 4 on the air side (not shown).

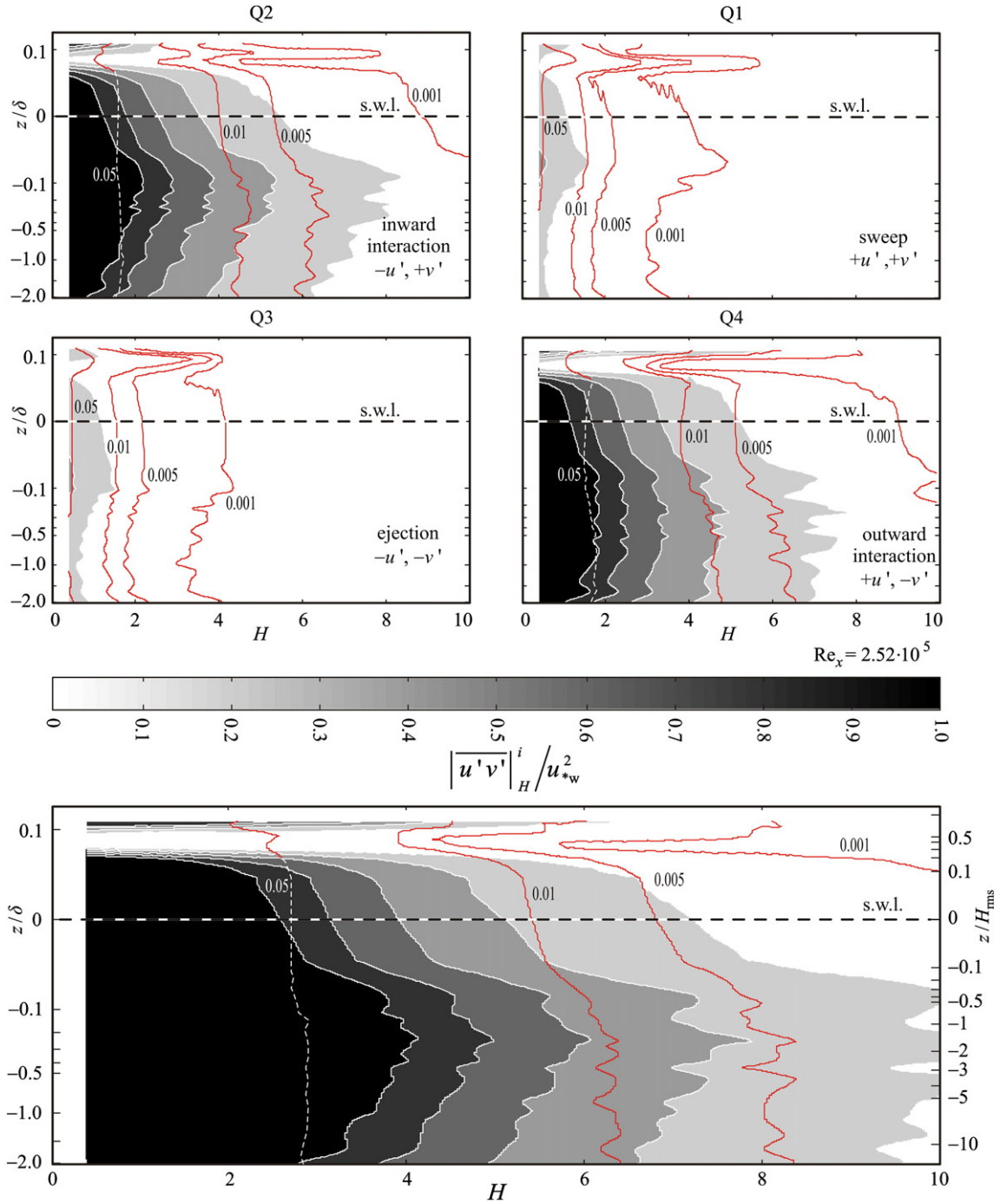

Fig. 13. Measurements in water, Section S0. Time-averaged Reynolds shear stress in each quadrant decomposed (upper panels) and without decomposition (lower panel) with increasing threshold *H*. The isolines of duration fraction are superimposed.

These preliminary remarks refer to isotropic turbulence, and can be used to interpret the present experiments. Fig. 15 shows the principal axis angle of turbulence in water and in air for a single test. Far from the interface, the Reynolds stress tensor in water has principal axis at $\approx -40°$, which rotates to $-45°$ in the layer just beneath the interface. In air, the angle decreases upward from an initial value of $\approx -20°$ to $\approx -45°$ just outside the boundary layer. The axes are less misaligned, if the conditional statistics are considered. It is even less for the quadrant Q4 contribution ($\approx -35°$ is the first value measured above the still water level). Notably on the air side, the shear stress is not uniform in the vertical direction, and tends to significantly drop towards the outer stream. Hence, larger shear stress generates a stronger misalignment between the principal axes of the Reynolds stress tensor and the strain rate tensor.

The water boundary layer has axes of the Reynolds tensor almost collinear with the axes of the strain rate tensor. This behaviour requires an equi-partition of turbulence between the two measured components, which slightly evolves further beneath the interface.

In view of the principal axes angle and the ratio between the maximum and the minimum stresses, the air flow immediately above the interface behaves as a boundary layer, whereas the water flow resembles a wake.

Fig. 16 shows the principal axis angle of turbulence in water and in air for a single test and for increasing threshold. The larger the

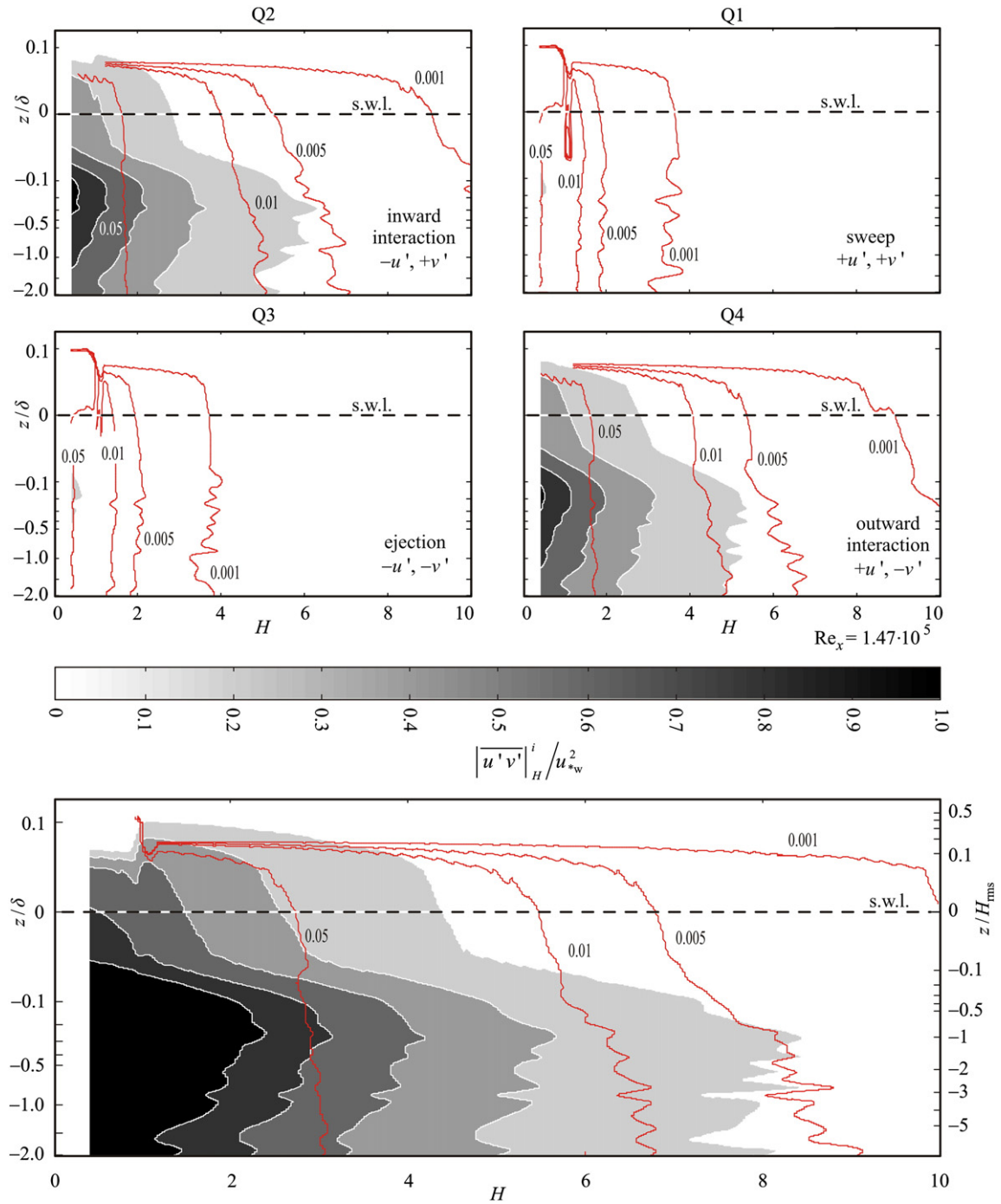

Fig. 14. Measurements in water, Section S3. Time-averaged Reynolds shear stress in each quadrant decomposed (upper panels) and without decomposition (lower panel) with increasing threshold H. The isolines of duration fraction are superimposed.

threshold the lower is the angle misalignment, with an asymptotic value which is different from zero.

6. A new description of the burst

Intensive studies of turbulent boundary layers have led to the recognition of coherent structures. This is manifested by formation streak patterns, lifting and oscillation of low-speed fluid, abrupt ejection of this low-speed fluid outward (this sequence of events is collectively known as bursting), and the strong motion of the outer, faster moving fluid towards the wall (sweep). Bursting is often described as a highly intermittent, explosive event. Intermittency is often with respect to time, however several experiments and numerical investigations (see Robinson, 1991, for a review) show that turbulent structures are more intermittent in space than in time. Once a coherent structure with a high level of turbulence intensity is produced, it moves in the fluid, presenting as a strong intermittent event for measurement at a fixed point. We expect that the probability of two subsequent strong events (e.g. $u'v'$ in the same quadrant over a threshold) as recorded by a fixed probe is generally high if there are coherent structures moving in the fluid. In order to analyse this aspect, a different description of burst is herein used. We assume

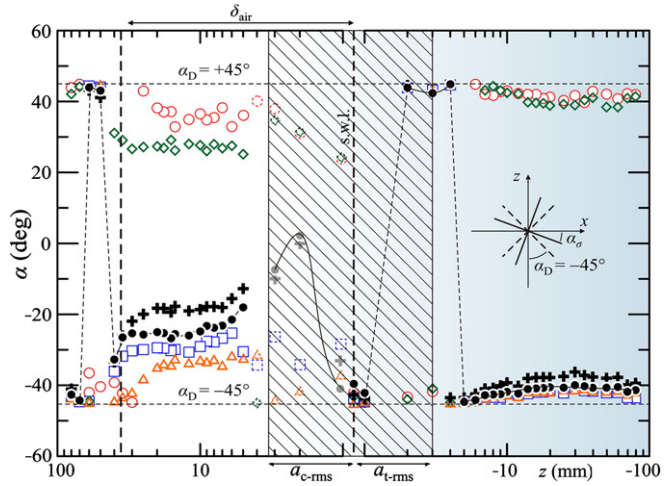

Fig. 15. Measurements in air over water and in water, Section S0. a) Time-averaged principal axes angle of the Reynolds stress tensor (+), with threshold $H=1$ (symbol ●) and quadrant decomposed with threshold $H=1$: ○ Q1, □ Q2 , ◇ Q3, △ Q4 . The dashed and grey symbols refer to measurement in water above the still water level. $a_{c\text{-}rms}$, $a_{t\text{-}rms}$ is the root mean square value of the crests, of the troughs.

that a burst can be characterized by a sequence of events in the same quadrant, amongst which at least one is over the threshold. The concept is similar to the grouping in water waves, where a sequence of waves moves as a group. Hence it is possible to classify isolated events (class 1), two subsequent events (class 2) etc., up to a maximum class depending on the length of measurements (for short measurements), the kind of turbulence field and the threshold. For each class, we can define the average duration of the elements and the average interval between two elements. This last variable is related to the frequency of bursting. It has been demonstrated (Blackwelder and Haritodinis, 1983) that the proper scales for bursting are the inner scale, namely the kinematic viscosity and the friction velocity, hence the non-dimensional frequency of bursting is $f^+ = f\nu/u^{*2}$. The results on the air side show a much lower frequency than those on the water side. At first, consideration should be given to the different sizes of the measurement volume (Blackwelder and Haritodinis, 1983). The non-dimensional length of the major axis of the volume in air is equal to $l_a^+ = lu_{*a}/\nu_a = 1.25\cdot10^{-3} \times 0.63/1.5\cdot10^{-5} = 52.5$ and is equal to $l_w^+ = lu_{*w}/\nu_w = 1.25\cdot10^{-3} \times 0.0258/10^{-6} = 32.3$ in water. Hence there is a stronger spatial filtering that reduces the number of events in air. Assuming that the reference length of the coherent structures responsible for bursting is $l^+ = 20$ and that the volume of measurements acts as a first-order filter, the corrected frequency is (Blackwelder and Haritodinis, 1983):

$$f_c^+ = f^+\left[1 + \left(\frac{l^+}{20}\right)^2\right]^{1/2}. \tag{25}$$

Applying this correction, the frequency measured in air is increased by a coefficient 2.81 and the frequency measured in air is increased by a coefficient 1.89.

The water side results at the two Sections S3 and S0 are shown in Fig. 17; the frequencies are not corrected for the size of the measurement volume. As long as the corrections for the length of the measurement volume are applied, the Reynolds number should not significantly affect the results. However, it is evident that the non-dimensional frequency increases by more than 50% from Section S3 to Section S0. Assuming that the uncertainties are similar in both sections, the difference has to be due to other phenomena, like the wave micro-breaking (Loewen and Siddiqui, 2006), which is a source of turbulent energy absent in conventional boundary layers. In Section S3, micro-breaking starts to take place, and correspondingly the wave height experiences a drop compared with the previous section, see Longo (2012). Micro-breaking is more pronounced in Section 0. Similar results are obtained for the other three quadrants. The maximum frequency is at a depth larger than H_{rms}, which appears to be a relevant scale for the turbulence on the water side.

7. Conclusions

This study details the structure of turbulence in the air-side and water-side boundary layers in wind generated waves.

- For both horizontal and vertical velocity fluctuations the value of the kurtosis is always greater than 3, which is the value for a normal distribution. These results hold true for measurements in both air over water and water, with higher values for the vertical velocity. The skewness for the horizontal velocity is negative for measurements in air over water except in the outer region, where the value of the Gaussian probability density distribution is reached. The skewness for the vertical velocity is always positive. The skewness for measurements in water is slightly negative for the horizontal velocity and slightly positive for the vertical velocity.
- The statistics of the angle between the instantaneous vertical fluctuation and the instantaneous horizontal velocity for measurements in air is similar to that obtained over solid wall. For measurements in

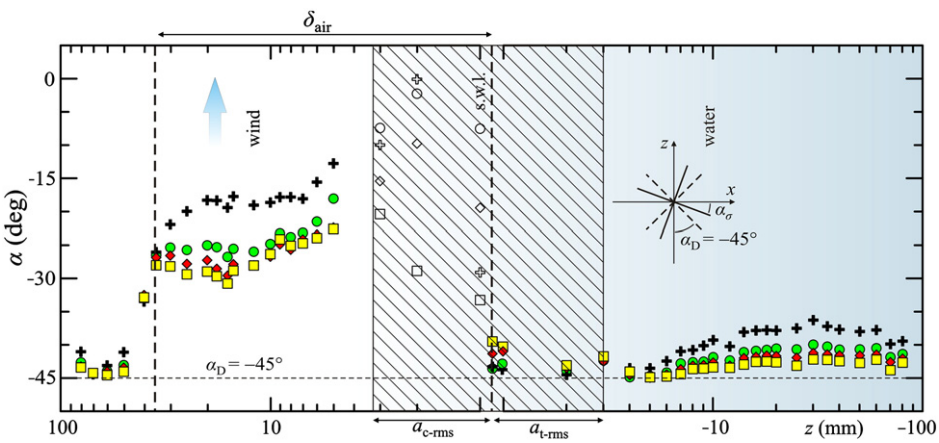

Fig. 16. Measurements in air and in water, Section S0. a) Time-averaged principal axes angle of the Reynolds stress tensor without threshold (symbol +), and with threshold $H=1$ (symbol ●), $H=2$ (symbol ◆), $H=3$ (symbol ■). The empty symbols refer to measurements in water above the still water level. $a_{c\text{-}rms}$, $a_{t\text{-}rms}$ is the root mean square value of the crests, of the troughs.

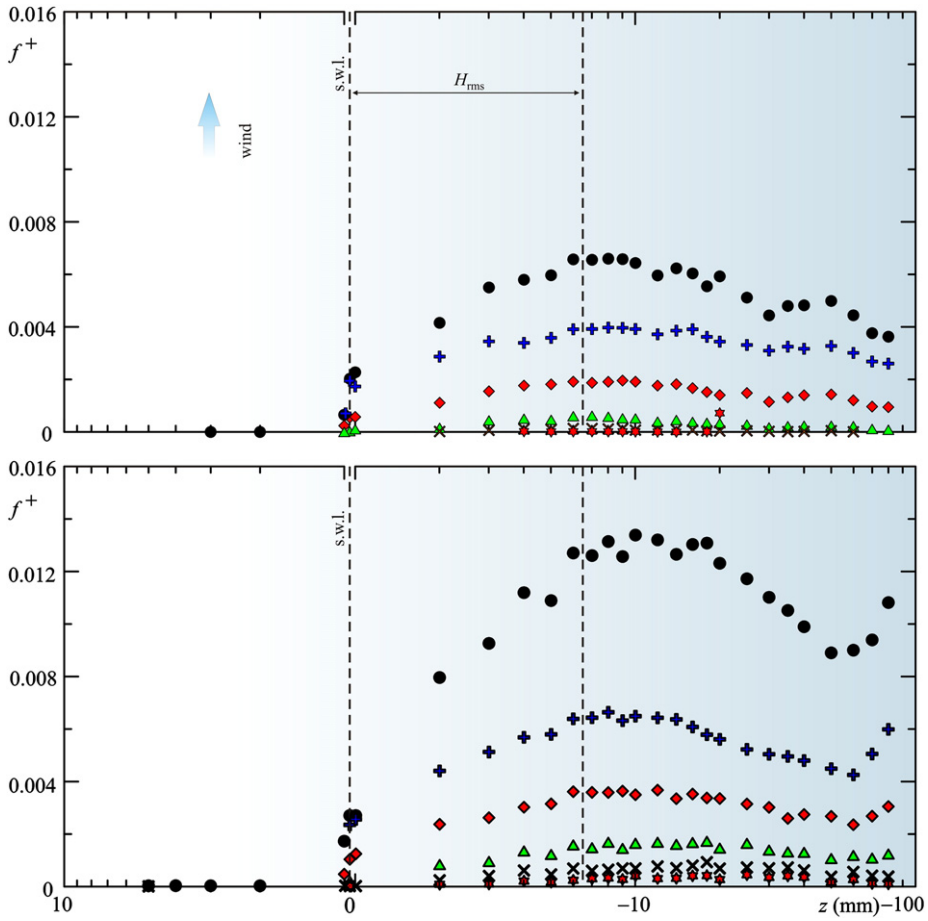

Fig. 17. Non-dimensional frequency of bursts event in Section S3 (upper panel) and Section S0 (lower panel), quadrant Q2. ● all bursts; ✚ bursts of length 1; ◆ bursts of length 2; ▲ bursts of length 3; × bursts of length 4; ✸ bursts of length 5.

water, it shows a large variance and the peak is biased towards negative angles.

- In the quadrants analysis, the contribution of quadrants Q2 and Q4 is dominant on both air side and water side. The nomenclature of the related coherent structures is sweeps and ejections on the air side, and becomes inward and outward interactions on the water side. The non-dimensional relative contributions and the concentration match fairly well near the interface. Sweeps in the air side (belonging to quadrant Q4) act directly on the interface and exert pressure fluctuations, which, in addition to the tangential stress and form drag, lead to the growth of the waves.
- The water drops detached from the crest and accelerated by the wind can play a major role in transferring momentum and in enhancing the turbulence level in the water side.
- On the air side, the Reynolds stress tensor's principal axes are not collinear with the strain rate tensor, and show an angle $\alpha_\sigma \approx -20°$ to $-25°$, while the angle of the strain rate tensor is $\alpha_D = \pm 45°$. This is similar to the orientation found in boundary layer and channel flows. On the water side, the angle is $\alpha_\sigma \approx -40°$ to $-45°$, similar to the angle found in wakes, and the angle of the strain rate tensor is still $\alpha_D = \pm 45°$. The ratio between the maximum and the minimum principal stresses is $\sigma_a/\sigma_b = 3$ to 4 on the air side and $\sigma_a/\sigma_b = 1.5$ to 3 on the water side. In this respect, the air side flow behaves like a classical boundary layer while the water side flow resembles a wake.
- The frequency of bursting on the water side shows a strong increment from Section S3 to Section S0, which the increase of fetch. It is attributed to micro-breaking effects, which are expected to be more important at larger fetches.

8. List of the symbols

$\overline{\cdots}$	time average operator
$\widetilde{\cdots}$	oscillating term operator
$\widehat{\cdots}$	phasic average operator
α_D	angle of the strain rate tensor principal axes
α_σ	angle of the Reynolds stress tensor principal axes
β_w, β_a, β_p	angle in water, in air, angle of peak occurrence
δ	boundary layer thickness
δ_1	displacement thickness of the boundary layer
δ_1/θ	shape factor of the boundary layer
ρ	mass density
θ	thickness of the boundary layer based on momentum
κ	turbulent kinetic energy
ν_a, ν_w	kinematic fluid viscosity of the air, of the water
$\sigma_{a,b}$	maximum, minimum principal stress
τ_{mb}	stress due to spray and detached drops
$a_{c\text{-}rms}$, $a_{t\text{-}rms}$	root mean square value of the crests, of the troughs
C	concentration, coefficient
C_f	friction coefficient
c_p, c_g	celerity of phase, of group
f^+, f_c, f_c^+	non-dimensional frequency (internal scales), corrected frequency, non-dimensional corrected frequency (internal scales)
f_p	peak frequency
H	wave height, threshold coefficient

H_{rms} root mean square wave height
k von Karman constant
k_s roughness length
l, l^+ length, non-dimensional length (internal scales)
L wave length
p.d.f., $p(\ldots)$ probability density function
Re, Re_x, Re_θ Reynolds number, based on the abscissa x, on momentum thickness
S_{ij} tensor of strain rate
S_H^i non-dimensional stress for the ith quadrant with threshold H
s.w.l. still water level
t time
U_∞ asymptotic wind velocity
U_s drift velocity
U, V streamwise, vertical wind velocity
U', V' streamwise, vertical fluctuating wind velocity
U_d velocity of the detached drops
u_∞ asymptotic water velocity
u, v streamwise, vertical water velocity
u', v' streamwise, vertical fluctuating water velocity
u'_{rms}, v'_{rms}
root mean square streamwise, vertical fluctuating water velocity
u_{*a} friction velocity in the air boundary layer
u_{*w} friction velocity in the water boundary layer
$W(\ldots)$ wake function
W_c wake coefficient
x, z spatial co-ordinates
z^+ non-dimensional vertical coordinate (internal scales)

Acknowledgements

The experimental data presented herein were obtained during the author's sabbatical leave at CEAMA, Grupo de Dinámica de Flujos Ambientales, University of Granada, Spain, kindly hosted by Miguel A. Losada. Financial support from CEAMA is gratefully acknowledged. Special thanks are given to Simona Bramato and Christian Mans, who provided great help with experiments.

References

Alfredsson, R.J., Johansson, A.V., 1984. On the detection of turbulence-generating events. Journal of Fluid Mechanics 139 (1), 325–345.
Andreas, E.L., 2004. Spray stress revisited. Journal of Physical Oceanography 34, 1429–1440.
Antonia, R.A., Bisset, D.K., Browne, L.W.B., 1990. Effect of Reynolds number on the topology of the organized motion in a turbulent boundary layer. Journal of Fluid Mechanics 213 (1), 267–286.
Blackwelder, R.F., Haritodinis, J.H., 1983. Scaling of the bursting frequency in turbulent boundary layers. Journal of Fluid Mechanics 132, 87–103.
Brocchini, M., Peregrine, D.H., 2001. The dynamics of strong turbulence at free surfaces. Part 1. Description. Journal of Fluid Mechanics 449, 225–254.
Camussi, R., Gui, G., 1997. Orthonormal wavelet decomposition of turbulent flows: intermittency and coherent structures. Journal of Fluid Mechanics 348, 177–199.
Champagne, F.H., Harris, V.G., Corrsin, S., 1970. Experiments on nearly homogeneous turbulent shear flow. Journal of Fluid Mechanics 41 (01), 81–139.
Chiapponi, L., Longo, S., Bramato, S., Mans, C., Losada, A.M., 2011. Free-surface turbulence, wind generated waves: laboratory data. Technical Report on Experimental Activity in Granada, University of Parma (Italy). CEAMA, Granada, Spain.
Donelan, M.A., 1998. Air–water exchange processes. In: Imberger, J. (Ed.), Physical Processes in Lakes and Oceans. : Coast. Estuar. Stud., 54. Am. Geophys. Union, Washington, DC, pp. 19–36.
Foster, R.C., Vianey, F., Drobinski, P., Carlotti, P., 2006. Near-surface coherent structures and the vertical momentum flux in a large-eddy simulation of the neutrally-stratified boundary layer. Boundary Layer Meteorology 120, 229–255.
Harris, V.G., Graham, J.A.H., Corrsin, S., 1977. Further experiments in nearly homogeneous turbulent shear flow. Journal of Fluid Mechanics 81 (4), 657–687.
Hunt, J.C.R., Stretch, D.D., Belcher, S.E., 2011. Viscous coupling of shear-free turbulence across nearly flat fluid interfaces. Journal of Fluid Mechanics 671 (iii), 96–120.
Kreplin, H., Eckelmann, H., 1979. Behavior of the three fluctuating velocity components in the wall region of a turbulent channel flow. Physics of Fluids 22 (7), 1233–1239.
Krostad, P.Å., Antonia, R.A., 1999. Surface roughness effects in turbulent boundary layers. Experiments in Fluids 27, 450–460.
Kudryavtsev, V.N., 2006. On the effect of sea drops on the atmospheric boundary layer. Journal of Geophysical Research 111, C07020.
Loewen, M.R., Siddiqui, M.H.K., 2006. Detecting microscale breaking waves. Measurement Science and Technology 17, 771–780.
Longo, S., 2012. Wind-generated water waves in a wind tunnel: free surface statistics wind friction and mean air flow properties. Coastal Engineering 61, 27–41.
Longo, S., Losada, M.A., 2012. Turbulent structure of air flow over wind-induced gravity waves. Experiments in Fluids, http://dx.doi.org/10.1007/s00348-012-1294-4 (published online since 30.3.2012).
Longo, S., Liang, D., Chiapponi, L., Aguilera Jiménez, L., 2012. Turbulent flow structure in experimental laboratory wind-generated gravity waves. Coastal Engineering 64, 1–15.
Nakagawa, S., Na, Y., Hanratty, T.J., 2003. Influence of a wavy boundary on turbulence. I. Highly rough surface. Experiments in Fluids 35, 422–436.
Nolan, K.P., Walsh, E.J., McEligot, D.M., 2010. Quadrant analysis of a transitional boundary layer subject to free-stream turbulence. Journal of Fluid Mechanics 658, 310–335.
Raupach, M.R., 1981. Conditional statistics of Reynolds stress in rough-wall and smooth-wall turbulent boundary layers. Journal of Fluid Mechanics 108, 363–382.
Robinson, S.K., 1991. Coherent motions in the turbulent boundary layer. Annual Review in Fluid Mechanics 23, 601–639.
Townsend, A.A., 1948. Local isotropy in the turbulent wake of a cylinder. Australian Journal of Scientific Research, Series A: Physical Sciences 1, 161–174.
Townsend, A.A., 1954. The uniform distortion of homogeneous turbulence. Quarterly Journal of Mechanics and Applied Mathematics 7 (1), 104–127.
Tucker, J., Reynolds, A.J., 1968. The distortion of turbulence by irrotational plane strain. Journal of Fluid Mechanics 32, 657–673.